Feature Article

Functional Materials Letters
Vol. 6, No. 4 (2013) 1330004 (5 pages)

DOI: 10.1142/S1793604713300041

World Scientific
www.worldscientific.com

SPACE-CHARGE LAYER, INTRINSIC "BULK" AND SURFACE COMPLEX DEFECTS IN ZnO NANOPARTICLES — A HIGH-FIELD ELECTRON PARAMAGNETIC RESONANCE ANALYSIS

RÜDIGER-A. EICHEL*,¶, EMRE ERDEM†, PETER JAKES*, ANDREW OZAROWSKI‡, JOHAN VAN TOL‡, RUDOLF C. HOFFMANN§ and JÖRG J. SCHNEIDER§

*Forschungszentrum Jülich, Institut für Energie- und Klimaforschung (IEK-9)
D-52425 Jülich, Germany

†Universität Freiburg, Institut für Physikalische Chemie
Albertstr. 21, D-79104 Freiburg, Germany

‡National High Magnetic Field Laboratory
Center for Interdisciplinary Magnetic Resonance
Florida State University, Tallahassee, Florida 32310

§Fachbereich Chemie, Eduard Zintl-Institut, Anorganische Chemie
TU Darmstadt, Petersenstrasse 18, 64287 Darmstadt, Germany
¶r.eichel@fz-juelich.de

Received 26 May 2013; Accepted 16 June 2013; Published 21 August 2013

The defect structure of ZnO nanoparticles is characterized by means of high-field electron paramagnetic resonance (EPR) spectroscopy. Different point and complex defects could be identified, located at the "bulk" or the surface region of the nanoparticles. In particular, by exploiting the enhanced g-value resolution at a Larmor frequency of 406.4 GHz, it could be shown that the resonance commonly observed at $g = 1.96$ is comprised of several overlapping resonances from different defects. Based on the high-field EPR analysis, the development of a space-charge layer could be monitored that consists of (shallow) donor-type $V_O^{\bullet}$ defects at the "bulk" and acceptor-type V'_{Zn} and complex $(Zn_i^{\bullet} - V'_{Zn})^{\times}$ defects at the surface. Application of a core-shell model allows to determine the thickness of the depletion layer to 1.0 nm for the here studied compounds [J.J. Schneider *et al.*, *Chem. Mater.* **22**, 2203 (2010)].

Keywords: ZnO nanoparticles; intrinsic defects; interstitial; vacancy; defect complex; high-field EPR.

1. Introduction

Recent research interest in nano-structured ZnO[1] is motivated by novel applications as electrode material for dye-sensitized solar cells,[2–4] light-emitting diodes,[5] photoluminescence,[6,7] thermoelectrics,[8] printable electronics[9] varistors[10,11] or sensors.[12] All of these applications exploit the semi-conducting properties of ZnO, which is a direct wide-bandgap (3.3 eV) semiconductor.[13] ZnO possesses a relatively open structure, with a hexagonal close packed lattice where Zn atoms occupy half of the tetrahedral sites and all of the octahedral sites are non-occupied. Hence, there are plenty of sites for ZnO to accommodate intrinsic defects, such as zinc interstitials or extrinsic dopants for instance. More generally, the semi-conducting properties of ZnO strongly depend on defects and the control of defect structure impacts the number of charge carriers. For that reason controlling the defect structure of ZnO is of paramount importance for the above-mentioned applications that exploit the wide range of properties of doped ZnO.

There are a number of intrinsic defect states within the bandgap of ZnO; the donor defects being zinc interstitials ($Zn_i^{\bullet\bullet}$, $Zn_i^{\bullet}$), and oxygen vacancies ($V_O^{\bullet\bullet}$, $V_O^{\bullet}$), whereas zinc vacancies rather form acceptor states (V''_{Zn}, V'_{Zn}). The also discussed $V_O^{\times}$, $V_{Zn}^{\times}$ and $Zn_i^{\times}$ rather present isovalent defects in the band gap. Zn interstitials and oxygen vacancies are known to be the predominant ionic defect types. However, which point and complex defect dominates in native, undoped ZnO is still a matter of great controversy.[14] The different defects are designated by using the standard *Kröger–Vink*

¶Corresponding author.

notation,[15] according to which the subscript indicates the lattice site that a defect occupies and the superscript corresponds to the electronic charge of the defect relative to the site that it occupies. To indicate isovalent substitution charge, $\times$ is used, $\bullet$ indicates a single positive charge, and $'$ signifies negative charge.

A sensitive means to study electronic and structural properties of various defects in ZnO is provided by electron paramagnetic resonance (EPR) spectroscopy.[16–19] The majority of the afore-mentioned defects are paramagnetic and thus accessible by EPR.[20] Different defects generally differ by their g-values but, however, the differences sometimes are very small such that the corresponding resonances overlap. Here we report on the application of high-field EPR with Larmor frequencies ranging between 9.8 and 406.4 GHz. Beside advantages in enhanced spectral resolution for high-spin functional centers,[21–23] we particularly exploit the markedly improved g-value resolution at 406.4 GHz.

2. Experimental Methods

Zinc oximate dihydrate was synthesized by Schiff-Base condensation of pyruvic acid and methoxylamine hydrochloride in aqueous solution followed by the addition of zinc nitrate hexahydrate. The raw product was recrystallized twice from distilled water. Analysis by inductive coupled plasma mass spectrometry (ICP-MS) showed that ubiquitous trace elements such as manganese were only present at a level of parts per million (ppm). For the preparation of zinc oxide nanoparticles a solution of the precursor in methoxyethanol with a concentration of 5 mass % was prepared. The solution was pressed through a syringe filter (Millipore, 200 nm) and filled in teflon vessels (Savillex, 120 mL in volume, 50 mm in diameter, maximum overpressure 5–6 bar). The conversion was performed by heating in a conventional kitchen microwave (800 W, 4 min). The nanoparticles were isolated by flocculation from the otherwise stable dispersions by addition of water and subsequent centrifugation. Finally, the particles were washed with acetone and distilled water and dried at 75°C in air. Transmission electron microscopy (TEM) was performed using a Tecnai G2 F20 (FEI) operating at 200 kV. Samples were prepared on lacy-carbon copper grid with 300 mesh. The obtained ZnO nanoparticles showed an almost-monomodal size distribution of about 50 nm (see e.g. Fig. 1).

X-band (9.85 GHz) continuous-wave EPR measurements were performed on a Bruker spectrometer (EMX), where the magnetic field was determined using a nuclear magnetic resonance gaussmeter (ER 035 M, Bruker), and, as a standard field marker, polycrystalline DPPH with $g = 2.0036$ was used for the exact determination of the magnetic field offset. Field-modulated continuous wave EPR experiments at high-frequencies (100–400 GHz) were performed at 298 K at the high magnetic field facility at the NHMFL, using a quartz synthesizer for the microwave (mw) radiation and a setup without resonator.[25]

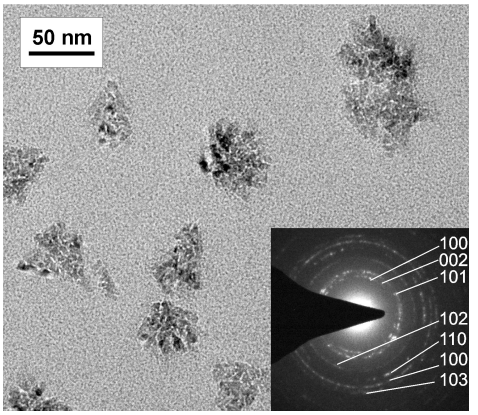

Fig. 1. TEM images of zinc oxide nanoparticles synthesized by microwave heating. The inset shows the indexed SAED pattern corresponding to the hexagonal zincite phase. (For further details see Ref. 9).

3. Theory

The spin Hamiltonian for a paramagnetic defect center with $S = \frac{1}{2}$ can be expressed by the electron Zeeman interaction[26]

$$\mathcal{H}_{S=\frac{1}{2}} = \beta_e \mathbf{B}_0 \cdot \mathbf{g} \cdot \mathbf{S}, \tag{1}$$

where g is the electron g-factor, β_e is the Bohr magneton and $\mathbf{B}_0$ denotes the external field, given in the principal axes system of the $\mathbf{g}$-matrix.

On the other hand, the spin-pair Hamiltonian describing the interaction between two electron spins with local spin $S_1 = S_2 = \frac{1}{2}$ has to consider additional terms, such that the corresponding spin-Hamiltonian is written as[27]

$$\mathcal{H}_{S=1} = \beta_e \sum_{i=1}^{2} \mathbf{B}_0 \cdot \mathbf{g} \cdot \mathbf{S}_i - J\mathbf{S}_1 \cdot \mathbf{S}_2 + \mathbf{S}_1 \cdot \mathbf{D} \cdot \mathbf{S}_2. \tag{2}$$

The last two terms describe the *isotropic* Heisenberg and the *anisotropic* dipolar spin-exchange interactions, respectively. In that notation, J is the isotropic exchange constant and $\mathbf{D}$ is the fine-structure tensor that combines contributions from anisotropic exchange interaction (D_{ex}) and magnetic dipole–dipole interactions (D_{dd}). The fine-structure interaction is commonly parameterized in terms of the sum $\sum_{k=2,\ldots,2S}^{-q \le k \le q} B_k^q O_k^q(S_x, S_y, S_z)$, with B_k^q the fine-structure Hamiltonian coefficients, and O_k^q the extended Stevens spin operators.

4. Results and Discussion

In order to characterize the intrinsic defects of nano-scale ZnO, EPR at various Larmor frequencies between X-band (9.85 GHz)

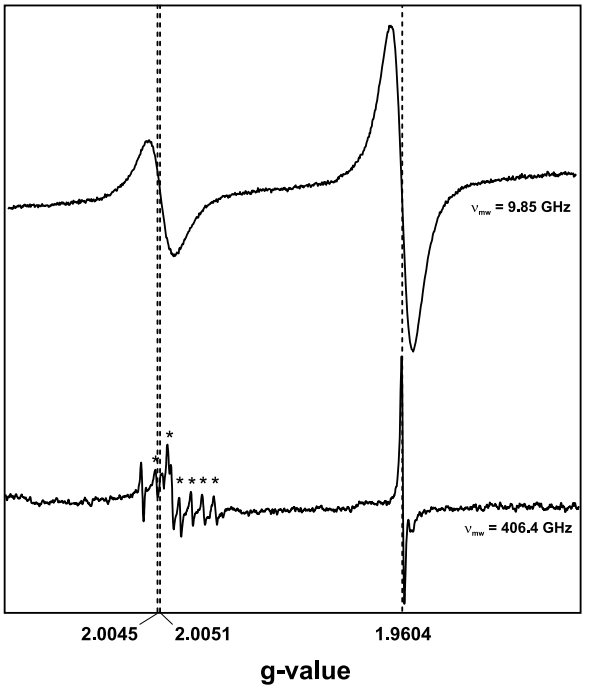

Fig. 2. EPR spectra of nano-scale ZnO recorded at 290 K in a g-value representation. X-band spectrum at a Larmor frequency of 9.85 GHz (top) compared to high-field EPR at a Larmor frequency of 406.4 GHz. The sextet hyperfine resonances owing to an Mn^{2+}-impurity center are indicated by asterisks.

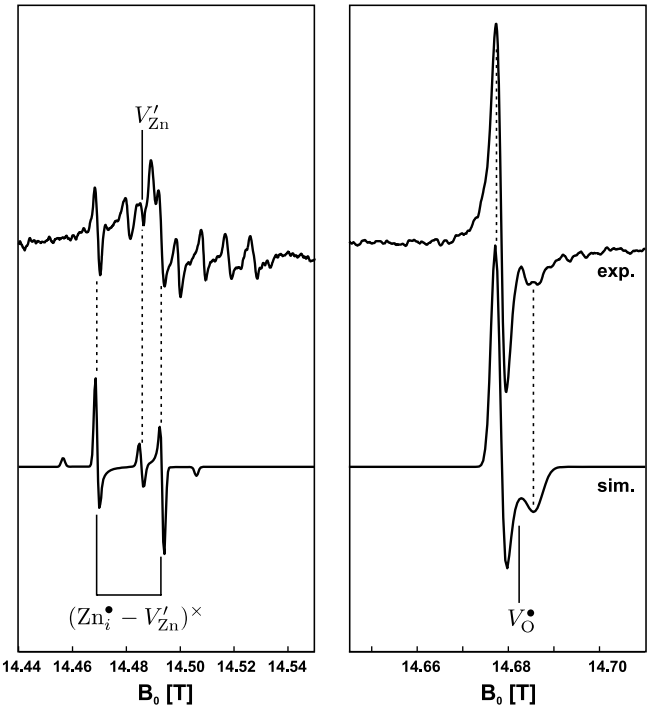

Fig. 3. High-field EPR spectrum of nano-scale ZnO at Larmor frequency of 406.4 GHz recorded at 290 K. Experimental spectrum (top) compared to numerical spectrum simulation (bottom) invoking the spin-Hamiltonian parameters given in Table 1.

and 406.4 GHz has been performed. The corresponding X-band and high-frequency ($\nu_{mw} = 406.4$ GHz) spectra are shown in Fig. 2 clearly demonstrating the benefit of high-field EPR by disentangling overlapping contributions with small g-value differences. In that respect, the two isotropic resonances observed at X-band, are resolved to at least three different lines at low field and an anisotropic line at high field.

The origin of the signal at $g \approx 1.96$ is generally explained by the existence of singly charged oxygen vacancies,[28–30] where the $V_O^{\bullet}$ act as *shallow donor* centers. Furthermore, the intensity of the resonance correlates with the sample electroconductivity.[32] Whereas the X-band spectrum exhibits an isotropic line shape for this resonance, at high Larmor frequency, a small axial g-anisotropy can be resolved [see e.g. Fig. 3(b)], which designates an axial site symmetry for the $V_O^{\bullet}$. This observation is consistent with recent *ab initio* calculations.[33]

A particular advantage of an EPR analysis is the ability to deduce relevant information on the nature and concentration of (paramagnetic) defect states (see e.g. Refs. 34– 36). The $V_O^{\bullet}$ are a result of the "bulk" defect chemistry of ZnO, after which oxygen vacancies arise from the *Schottky*-type defect equilibrium

$$Zn_{Zn}^{\times} + O_O^{\times} \rightleftharpoons V''_{Zn} + V_O^{\bullet\bullet} + Zn_i^{\times} + \frac{1}{2}O_2(g), \qquad (3)$$

whereas molecular oxygen evaporates to the atmosphere during high-temperature processing, the zinc atoms rather form interstitials. Concerning the oxygen vacancies, different ionization equilibria allow various charge states, where only the singly-charged $V_O^{\bullet}$ is paramagnetic ($S = \frac{1}{2}$)

$$V_O^{\times} \rightleftharpoons V_O^{\bullet} + e', \qquad (4)$$

$$V_O^{\bullet} \rightleftharpoons V_O^{\bullet\bullet} + e'. \qquad (5)$$

On the other hand, at $g \approx 2.0$ the single resonance observed at X-band transforms into a manifold of resonance lines at 406.4 GHz, demonstrating that different defects are simultaneously present. The sextet hyperfine pattern owing a ^{55}Mn defect center with $g_{Mn^{2+}} = 2.0019$ and $^{55Mn}A = 260$ MHz, is indicative for a divalent oxidation state[41–43] and thus isovalent substitution of the Mn^{2+} for the Zn-site ($Mn_{Zn}^{\times}$). The corresponding resonances are marked with asterisks. The origin of the $Mn_{Zn}^{\times}$-center are spurious contaminants in the raw materials with concentrations in the ppm region.

Beside the Mn sextet hyperfine pattern, three distinct additional resonances are resolved, where the two outer resonances show identical intensity. Principally, this observation may be explained by three different scenarios: first, this "doublet" may be due to two different paramagnetic species of different g-value. In this case, the splitting between the lines should be field dependent. Because the splitting of the doublet remained invariant upon changing the Larmor frequency from 300 to 400 GHz (not shown), this scenario

can be ruled out. Accordingly, a field-independent interaction has to be the origin of the observed doublet, which could be either owing to a hyperfine interaction with a magnetically active nucleus of nuclear spin $I = \frac{1}{2}$ or due to a triplet state with electron spin $S = 1$. However, as the observed splitting between the lines is orders of magnitude larger than the one reported for the hyperfine interactions of ^{1}H-impurities,[18,31] this model can be discarded as well. Correspondingly, the origin of the observed doublet is due a triplet $S = 1$ state.

Concerning the defect-structural origin of the resonances about $g \approx 2.0$, it was recently demonstrated that these signals are owing to surface defects.[9,32,40] Commonly, oxygen vacancies are depleted at the surface layers[10] and defects at the surface are rather attributed to zinc interstitials or zinc vacancies.[16] Additional to the interstitials formed according to the Schottky-type defect equilibrium (3), zinc interstitials and zinc vacancies are generated owing to a *Frenkel*-type defect equilibrium according to

$$\mathrm{Zn}_{\mathrm{Zn}}^{\times} \rightleftharpoons V_{\mathrm{Zn}}^{\times} + \mathrm{Zn}_i^{\times}. \tag{6}$$

Subsequent ionization equilibria again allow for varying charge states

$$V_{\mathrm{Zn}}^{\times} \rightleftharpoons V_{\mathrm{Zn}}' + h^{\bullet}, \tag{7}$$

$$V_{\mathrm{Zn}}' \rightleftharpoons V_{\mathrm{Zn}}'' + h^{\bullet}, \tag{8}$$

$$\mathrm{Zn}_i^{\times} \rightleftharpoons \mathrm{Zn}_i^{\bullet} + e', \tag{9}$$

$$\mathrm{Zn}_i^{\bullet} \rightleftharpoons \mathrm{Zn}_i^{\bullet\bullet} + e'. \tag{10}$$

We assign the resonance at $g = 2.0045$ to a singly-charged V_{Zn}'.[16] Because all of the intrinsic defects in ZnO bear an electron spin of $S = \frac{1}{2}$, the only explanation for a triplet state with $S = 1$ is a complexation of two defects with $S = \frac{1}{2}$. Exploiting the Frenkel-type defect equilibrium (6), we propose the formation of a $(\mathrm{Zn}_i^{\bullet} - V_{\mathrm{Zn}}')^{\times}$ defect complex, where the zinc ion that leaves a lattice site occupies an interstitial position in the first coordination sphere of the initial site

$$\mathrm{Zn}_i^{\bullet} + V_{\mathrm{Zn}}' \rightleftharpoons (\mathrm{Zn}_i^{\bullet} - V_{\mathrm{Zn}}')^{\times}. \tag{11}$$

Because both isolated defects mutually compensate when forming the defect complex, the corresponding $(\mathrm{Zn}_i^{\bullet} - V_{\mathrm{Zn}}')^{\times}$ defect complex is electrically neutral. The assignment of defect-complex formation is supported by recent photoluminescence experiments that anticipated the existence of complex defects involving zinc interstitials to explain green emission bands in the corresponding spectra,[6] in contrast to the blue emission that is assigned to the electron transition from shallow-donor $\mathrm{Zn}_i^{\bullet}$ point-defects.[37] The existence of such $(\mathrm{Zn}_i^{\bullet} - V_{\mathrm{Zn}}')^{\times}$ defect complexes is in line with results reported for ZnSe[38] and may be compared to donor−acceptor pair centers recently reported in Li-doped ZnO nanocrystals.[39] This assignment is furthermore in line with the more general trend that oppositely charged defects tend to form defect complexes in oxide compounds.[45–48]

Table 1. Refined set of spin-Hamiltonian parameters obtained after numerical spectrum simulation of the high-field EPR spectrum (Fig. 3).

	$V_{\mathrm{O}}^{\bullet}$	V_{Zn}'	$(\mathrm{Zn}_i^{\bullet} - V_{\mathrm{Zn}}')^{\times}$	$\mathrm{Mn}_{\mathrm{Zn}}^{\times}$
g_{iso}	—	2.0045	2.0051	2.0019
$g_{\parallel}$	1.97715	—	—	—
$g_{\perp}$	1.97825	—	—	—
B_2^0 [GHz]	—	—	1.39	—
A [MHz]	—	—	—	260

Taking the above derived defect structure into account, the obtained high-field spectrum can accurately be numerically simulated as demonstrated in Fig. 3. The corresponding refined set of spin-Hamiltonian parameters is summarized in Table 1.

For the here studied nanostructured ZnO compounds, the confined length scales and accordingly enlarged surface-to-volume ratio promotes surface defects to play a stronger role in controlling materials properties. Most recently this effect has been interpreted in terms of a "*core-shell*" model in which the particles consist of a core region that is electronically different from the surface of the ZnO nanoparticles.[9,19] Exploiting the above-derived defect structure, the core is dominated rather by (shallow) donor-type $V_{\mathrm{O}}^{\bullet}$, whereas at the surface acceptor-type V_{Zn}' and $(\mathrm{Zn}_i^{\bullet} - V_{\mathrm{Zn}}')^{\times}$ prevail. As consequence, the development of a *space-charge (depletion) layer* as schematically illustrated in Fig. 4 emerges, which clarifies the defect structure anticipated for a grain-boundary defect model.[49] In particular, application of the core-shell model allows to determine the thickness of the depletion layer to 1.0 nm for the here studied compounds.[19] Together with the newly proposed $(\mathrm{Zn}_i^{\bullet} - V_{\mathrm{Zn}}')^{\times}$ defect complex, this provides a means to discuss the manifold materials properties of nano-structured ZnO for novel applications.[2,5,6,8,12]

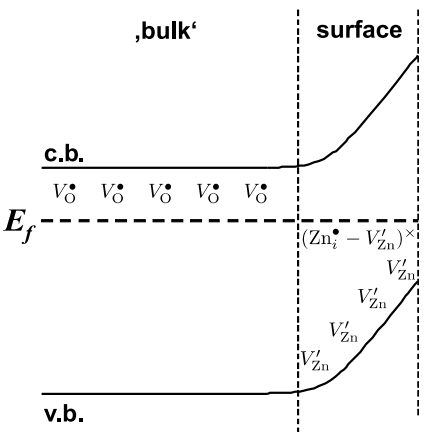

Fig. 4. Schematical illustration of the development of a space-charge layer as function of the defect structure in nano-sized ZnO. Fermi energy (E_f), conduction (c.b.) and valence (v.b.) are indicated.

Acknowledgments

This research has been supported by the NHMFL, which is funded by the NSF through the Cooperative Agreement No. DMR-0654118, the State of Florida and the DOE. TEM investigations were performed by J. Engstler (TU Darmstadt) at the Ernst-Ruska Centre (ERC), Jülich, under project co-operation ERC-TUD1.

References

1. X. Zhao *et al.*, *Funct. Mater. Lett.* **1**, 167 (2008).
2. K. Keis *et al.*, *Sol. Energy Mater. Sol. Cells* **73**, 51 (2002).
3. X. D. Gao *et al.*, *Funct. Mater. Lett.* **2**, 27 (2009).
4. L. Guo *et al.*, *Funct. Mater. Lett.* **3**, 279 (2010).
5. J. Bao *et al.*, *Nano Lett.* **6**, 1719 (2006).
6. A. B. Djurisic *et al.*, *Adv. Funct. Mat.* **14**, 856 (2004).
7. S. Dhara *et al.*, *Funct. Mat. Lett.* **4**, 25 (2011).
8. Y. Kinemuchi *et al.*, *J. Electron. Mater.* **39**, 2059 (2010).
9. J. J. Schneider *et al.*, *J. Mater. Chem.* **19**, 1449 (2009).
10. G. D. Mahan, *J. Appl. Phys.* **54**, 3825 (1983).
11. T. K. Gupta, *J. Am. Ceram. Soc.* **7**3, 1817 (1990).
12. M. Yang *et al.*, *Sens. Actuators B* **117**, 80 (2006).
13. Ü. Özgür *et al.*, *Appl. Phys. Rev.* **98**, 041301 (2005).
14. K. I. Hagemark, *J. Solid State Chem.* **16**, 293 (1976).
15. F. A. Kröger and H. J. Vink, *Solid State Phys.* **3**, 273301 (1956).
16. A. Pöppl and G. Völkel, *Phys. Stat. Sol.* (a) **115**, 247 (1989). *ibid. Phys. Stat. Sol.* (a) **125**, 571 (1991).
17. B. K. Meyer *et al.*, *Phys. Stat. Sol.* (b) **241**, 231 (2004).
18. S. B. Orlinskii *et al.*, *Phys. Rev. Lett.* **94**, 097602 (2005).
19. J. J. Schneider *et al.*, *Chem. Mater.* **22**, 2203 (2010).
20. R.-A. Eichel, *Phys. Chem. Chem. Phys.* **13**, 368 (2011).
21. R.-A. Eichel *et al.*, *Appl. Phys. Lett.* **88**, 122506 (2006).
22. E. Erdem *et al.*, *Phys. Scr. T* **129**, 12 (2007).
23. P. Jakes *et al.*, *Phys. Chem. Chem. Phys.* **13**, 9344 (2011).
24. M. R. Hill *et al.*, *Inorg. Chim. Acta* **358**, 201 (2005).
25. J. van Tol *et al.*, *Rev. Sci. Instrum.* **76**, 074101 (2005).
26. A. Abragam and B. Bleaney, *Electron Paramagnetic Resonance of Transition Ions*, (Clarendon Press, Oxford, 1970).
27. A. Bencini and D. Gatteschi, *EPR of Exchange-Coupled Systems*, (Springer, Heidelberg, 1990).
28. K. Vanheusden *et al.*, *Appl. Phys. Lett.* **68**, 403 (1996).
29. N. G. Kakazey *et al.*, *J. Mater. Sci.* **32**, 4619 (2002).
30. S. M. Evans *et al.*, *J. Appl. Phys.* **103**, 043710 (2008).
31. D. M. Hoffman *et al.*, *Phys. Rev. Lett.* **88**, 045504 (2002).
32. Y. Hu and H. J. Chen, *J. Nanopart. Res.* **10**, 401 (2008).
33. P. Erhart *et al.*, *Phys. Rev. B* **73**, 205203 (2006).
34. E. Erdem *et al.*, *J. Phys.: Condens. Matter* **22**, 345901 (2010).
35. M. D. Drahus *et al.*, *Solid State Ion.* **184**, 47 (2011).
36. P. Jakes *et al.*, *Chem. Phys. Chem.* **12**, 3578 (2011).
37. G. N. He *et al.*, *Funct. Mater. Lett.* **3**, 107 (2010).
38. F. C. Rong *et al.*, *Phys. Rev. B* **54**, 7779 (1996).
39. S. B. Orlinskii *et al.*, *Phys. Rev. B* **74**, 045204 (2006).
40. B. Yu *et al.*, *Matter Lett.* **33**, 247 (1998).
41. L. X. Zhang *et al.*, *Appl. Phys. Lett.* **93**, 202901 (2008).
42. E. Aksel *et al.*, *J. Am. Ceram. Soc.* **94**, 1363 (2011).
43. M. D. Drahus *et al.*, *Phys. Rev B* **84**, 064113 (2011).
44. J. Han *et al.*, *J. Eur. Ceram. Soc.* **22**, 49 (2002).
45. R.-A. Eichel *et al.*, *Phys. Rev. Lett.* **100**, 095504 (2008).
46. R.-A. Eichel *et al.*, *Phys. Chem. Chem. Phys.* **11**, 8698 (2009).
47. E. Erdem *et al.*, *Funct. Mat. Lett.* **3**, 65 (2010).
48. E. Erünal *et al.*, *Phys. Rev. B* **84**, 184113 (2011).
49. T. K. Gupta and W. G. Carlson, *J. Mater. Sci.* **20**, 3487 (1985).